Geophysical Journal International

Geophys. J. Int. (2021) **226,** 536–547
Advance Access publication 2021 March 19
GJI Seismology

doi: 10.1093/gji/ggab109

3-D attenuation image of fluid storage and tectonic interactions across the Pollino fault network

P. Sketsiou [1], L. De Siena [1,2] S. Gabrielli [1,3] and F. Napolitano[4]

[1] *School of Geosciences, University of Aberdeen, Aberdeen AB*24 3*UE, Scotland, UK. E-mail: panayiotasketsiou@gmail.com*
[2] *Institute of Geosciences, Johannes Gutenberg University, D-*55128 *Mainz, Germany*
[3] *Instituto Nazionale di Geofisica e Vulcanologia (INGV),* 00143 *Rome, Italy*
[4] *Dipartimento di Fisica "E.R.Caianiello", Universitá degli Studi di Salerno,* 84084 *Fisciano (SA), Italy*

Accepted 2021 March 17. Received 2021 February 19; in original form 2020 October 14

SUMMARY

The Pollino range is a region of slow deformation where earthquakes generally nucleate on low-angle normal faults. Recent studies have mapped fault structures and identified fluid-related dynamics responsible for historical and recent seismicity in the area. Here, we apply the coda-normalization method at multiple frequencies and scales to image the 3-D *P*-wave attenuation (Q_P) properties of its slowly deforming fault network. The wide-scale average attenuation properties of the Pollino range are typical for a stable continental block, with a dependence of Q_P on frequency of $Q_P^{-1} = (0.0011 \pm 0.0008) f^{(0.36 \pm 0.32)}$. Using only waveforms comprised in the area of seismic swarms, the dependence of attenuation on frequency increases [$Q_P^{-1} = (0.0373 \pm 0.0011) f^{(-0.59 \pm 0.01)}$], as expected when targeting seismically active faults. A shallow very-low-attenuation anomaly (max depth of 4–5 km) caps the seismicity recorded within the western cluster 1 of the Pollino seismic sequence (2012, maximum magnitude $M_w = 5.1$). High-attenuation volumes below this anomaly are likely related to fluid storage and comprise the western and northern portions of cluster 1 and the Mercure basin. These anomalies are constrained to the NW by a sharp low-attenuation interface, corresponding to the transition towards the eastern unit of the Apennine Platform under the Lauria mountains. The low-seismicity volume between cluster 1 and cluster 2 (maximum magnitude $M_w = 4.3$, east of the primary) shows diffuse low-to-average attenuation features. There is no clear indication of fluid-filled pathways between the two clusters resolvable at our resolution. In this volume, the attenuation values are anyway lower than in recognized low-attenuation blocks, like the Lauria Mountain and Pollino Range. As the volume develops in a region marked at surface by small-scale cross-faulting, it suggests no actual barrier between clusters, more likely a system of small locked fault patches that can break in the future. Our model loses resolution at depth, but it can still resolve a 5-to-15-km-deep high-attenuation anomaly that underlies the Castrovillari basin. This anomaly is an ideal deep source for the SE-to-NW migration of historical seismicity. Our novel deep structural maps support the hypothesis that the Pollino sequence has been caused by a mechanism of deep and lateral fluid-induced migration.

Key words: Body Waves; Seismic attenuation; Seismic tomography; Fractures, faults, and high strain deformation zones.

1 INTRODUCTION

Seismic waves lose energy during propagation in heterogeneous Earth media. They lose amplitude in space and time due to *seismic attenuation*, whose description is central when modelling seismic wave propagation both at the laboratory and field scales (Müller *et al.* 2010; Cormier 2011; Sato *et al.* 2012). The total quality factor (Q) measures the anelastic attenuation of coherent waves. It is defined as the fractional energy lost per cycle and controls the decay of the energy density spectrum with lapse time from the origin time of the earthquake (Cormier 2011). While in many seismological studies the physical processes measured by Q (e.g. scattering and absorption) are considered a hindrance and removed, the attenuation of body, surface and coda waves has become a

fundamental attribute to image heterogeneous Earth structures (Quan & Harris 1997; Romanowicz 1998; Schurr *et al.* 2003; De Siena *et al.* 2010; Mayor *et al.* 2016; Prudencio & Manga 2019). Q is suited to image fluid storage and propagation at subduction (Schurr *et al.* 2003) and, especially, fault scale (Chiarabba *et al.* 2009).

The most widely used method to estimate the attenuation of seismic waves is the so-called t^* method (Romanowicz 1998; Schurr *et al.* 2003), where t^* represents the cumulative attenuation along a ray path (Kanamori 1967). The t^* method measures the high-frequency spectral decay rate above the corner frequency (dependent on earthquake magnitude) for each waveform: $e^{-\omega t^*/2}$ (Cormier 1982; Bindi *et al.* 2006), where ω is the angular frequency. While its application is easy and justifiable in the presence of gradually varying heterogeneity, the assumptions underlying the method are often unfulfilled if there are strong velocity variations, interference between coherent waves, and complex source and site spectra (Del Pezzo 2008; De Siena *et al.* 2009; Parolai *et al.* 2015). The method does not allow a frequency-dependent reconstruction of structures, even if these certainly interact differently with seismic waves depending on sampling frequency.

Aki & Chouet (1975) and Rautian & Khalturin (1978) developed the *coda normalization* as an alternative method to measure Q of S waves (Q_S) within highly heterogeneous lithospheric media. Yoshimoto *et al.* (1993) extended the method to measure the attenuation of P waves (Q_P), normalizing P-wave energy by S-coda energy. The effect of different radiation patterns on coda-normalized measurements is negligible if the data set consists of events with a wide range of epicentral distances that allow to average over many focal mechanisms (Yoshimoto *et al.* 1993). Even considering single-station measurements, radiation patterns only have secondary effects if the window taken to measure direct-wave amplitudes is long enough. Takemura *et al.* (2009) studied the distortion of the S-wave radiation pattern of small-magnitude earthquakes due to small-scale crustal heterogeneity. They concluded that the S-wave radiation distributes quasi-isotropically for high-frequency waves after a few mean-free times from the origin-time of the earthquake. Obviously, when enlarging the window used to measure P-wave amplitudes, the risk is to include spurious surface phases, finally losing focus on the infinite-frequency *seismic ray*. A preliminary measurement of spatially varying coda properties is also necessary (De Siena *et al.* 2014a).

The coda normalization method is a standard for measuring and mapping the average attenuation properties of the lithosphere. Examples comprise the comparison of shear wave attenuation in different areas of the crust (Frankel *et al.* 1990) and collision zones (Sharma *et al.* 2007; Parvez *et al.* 2012). Del Pezzo *et al.* (2006) first developed an attenuation tomography method based on coda normalization (CN) to image Mount Vesuvius. They measured Q_S along rays traced in a velocity model to invert for the 3-D attenuation structure of the volcano. De Siena *et al.* (2009) benchmarked the method against t^*, obtaining a multiple resolution 3-D model of both Q_S and Q_P at the same volcano, using a direct-wave time window of 3 s to remove radiation pattern effects. At Campi Flegrei caldera, where topographic effects are marginal, the window length was reduced to 2 s (De Siena *et al.* 2010). Since then, body-wave attenuation models based on the CN method have been applied at crustal scale across the world, becoming a standard in volcanoes (Matsumoto *et al.* 2009; De Siena *et al.* 2014b; Prudencio *et al.* 2015a, b; De Siena *et al.* 2017; Nazemi *et al.* 2017; Prudencio & Manga 2019).

While the coda-normalization method has been used to study the average attenuation properties of fault zones (Akinci & Eyidoğan 1996) a 3-D tomographic inversion has never been applied in this setting. De Siena *et al.* (2014a) have published *MuRAT*, a MATLAB® code to obtain frequency-dependent Q_P and Q_S measurements using the CN method and invert for the P- and S-wave attenuation structures of highly heterogeneous regions. In its 2.0 version, the code allows to estimate coda attenuation before normalization, reducing the unknowns in the inversion.

2 STRUCTURE AND DYNAMICS OF THE POLLINO FAULT NETWORK

The data in the present work have been recently used to map the 2-D frequency-dependent spatial variations in scattering and absorption across the Pollino fault network (Napolitano *et al.* 2020a). This fault network comprises low-angle, E- and NNE-dipping faults, as well as antithetic, high-angle, SW- to WSW-dipping faults (Brozzetti *et al.* 2017). The area is historically recognized as a seismic gap in the Apennines chain (Passarelli *et al.* 2015). Regardless, there is a record of historical earthquakes with magnitudes between 5.2–6.0 dating back to the seventeenth century (Tertulliani & Cucci 2014). The Pollino seismic sequence has occurred between 2010 and 2014 within the gap and with a highly variable rate.

The activity started in Fall 2010, with a small cluster of events, which faded out in Spring 2011 and started again in Fall 2011, located in the SE part of the Mercure Basin. In May 2012, an event with $M_w = 4.3$ occurred to the east of the first sequence, with a classical main shock–aftershock sequence (hereafter "cluster 2", as labelled in Fig. 1). In July 2012, the activity restarted in the first location, in the SE of the Mercure Basin, lasting several months, with a peak $M_w = 5.1$ normal faulting event occurring on 2012 October 25. Although the seismicity gradually faded by Spring 2012, the seismicity rate was higher than usual until 2014. The seismic activity in this location will be hereafter called 'cluster 1'. These sequences comprised thousands of low-magnitude earthquakes but no main shock–aftershock succession (Passarelli *et al.* 2015; Totaro *et al.* 2015; Ferranti *et al.* 2017). Such features, together with the occurrence of slow-slip earthquakes (Cheloni *et al.* 2017), have supported the identification of Pollino as a region of slow deformation. This slow-slip event, equivalent to an $M_W \sim 5.5$, has been detected between August 2012 and March 2013, and located in the same seismogenic volume of the first cluster. Increased pore pressure and, more generally, pressurized fluids modulating stress along the fault, are the most likely sources of slow-slip events and aseismic transients seismicity (Passarelli *et al.* 2015; Cheloni *et al.* 2017).

A frequency-dependent scattering and absorption mapping has provided the spatial measurements of coda attenuation necessary for the application of *MuRAT*2.0 (Napolitano *et al.* 2020a). This work has brought forward the hypothesis that lateral fluid migrations from the Castrovillari basin, SE of the fault network, is the most likely source of historical seismic events (Napolitano *et al.* 2020a; Sketsiou *et al.* 2020). Their high-scattering and high-absorption patterns shift towards NW following the strike of NW-to-SE-trending faults. The SE–NW migration stops at the boundary of the eastern unit of the Apennine Platform (Brozzetti *et al.* 2017) at intermediate frequencies. It marks the faults where the Pollino seismic sequence nucleated in the highest frequency range. Despite the increasing amount of shallow geological and geophysical information (Passarelli *et al.* 2015; Totaro *et al.* 2015; Brozzetti *et al.* 2017),

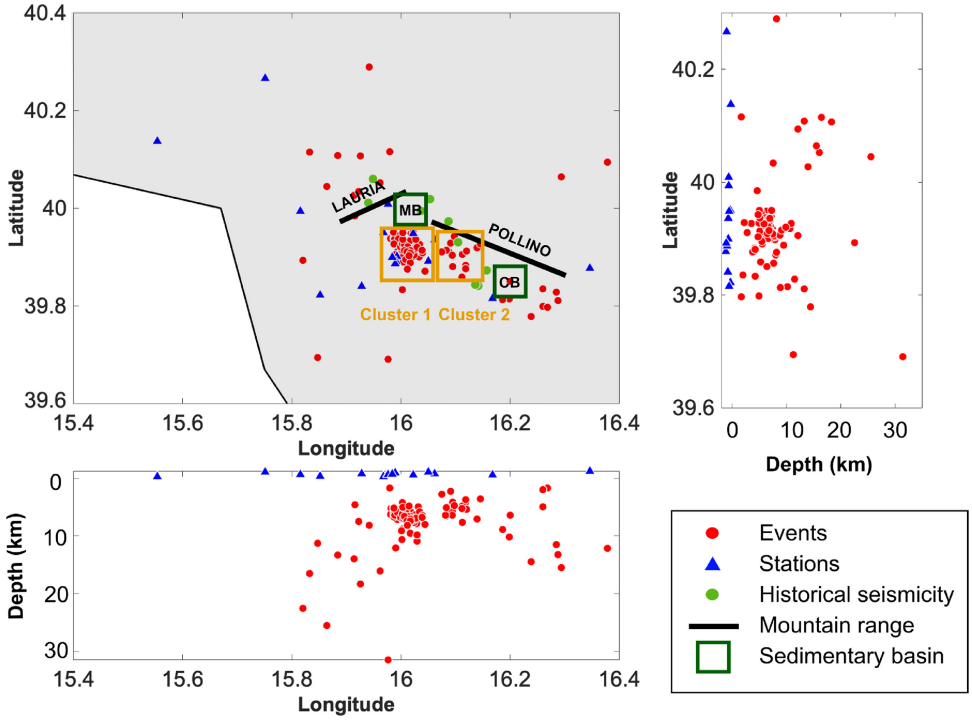

Figure 1. Map of the study area, showing the earthquakes used in this work (red circles) and the seismic stations (blue triangles). Historical seismicity is marked with green circles. Mountain ranges in the area are marked with solid black lines and the locations of two sedimentary basins, Mercure (MB) and Castrovillari (CB), are indicated by green squares. There are two clusters of events discussed in the paper, marked here by orange rectangles as cluster 1 (left) and cluster 2 (right).

leading to new models and hypotheses of the deep fault structures (Ferranti *et al.* 2017), deep 3-D geophysical models of the area are still lacking.

3 DATA

The data set consists of 102 earthquakes (for a total of 702 waveforms) that occurred between 2010 and 2014 in the seismogenic volume responsible for the Pollino seismic swarm-like sequence (Passarelli *et al.* 2015; Napolitano *et al.* 2020b) and nearby, as shown in Fig. 1. The waveforms have been recorded at 18 seismic stations operated by *Istituto Nazionale di Geofisica e Vulcanologia (INGV)*, *Universitá della Calabria* (Margheriti *et al.* 2013) and *GFZ, Potsdam, Germany* (Passarelli *et al.* 2012). The strongest events of this data set ($M_L > 2.7$) have been used to study the source mechanism and the development of the swarm (Totaro *et al.* 2015) and to constrain the geometry of the faults inferred by Brozzetti *et al.* (2017). Most of these waveforms have been used to assess ground-motion amplifications (Napolitano *et al.* 2018) and separation of scattering and absorption contribution to the total attenuation of coda waves (Napolitano *et al.* 2020a; Sketsiou *et al.* 2020). To study the *P*-wave attenuation, we selected the vertical component of the Pollino waveforms, characterized by source-receiver distances between 1 and 40 km, by local magnitude between 1.8 and 4.3, and depths between 1 and 32 km. The equipartition between *P* and *S* waves (Napolitano *et al.* 2020a) allows us to use the vertical component to compute coda waves at late lapse times, where the diffusion regime is reached (Sketsiou *et al.* 2020). The selected area, [lon: 15.4–16.4 (111 km); lat: 39.6–40.4 (70 km); depth: 20 km] was divided in blocks of 0.1°, a suitable size to solve a 3-D problem. For ray tracing, we interpolated the velocity model by Barberi *et al.* (2004) between depths of 0 and 70 km, tracing rays with a ray-bending approach (De Siena *et al.* 2014b).

We performed two different tomographic analyses, corresponding to two data sets. Data set 1 comprises all the waveforms described above to invert for the entire volume under consideration. Data set 2 is a selection of 647 waveforms chosen to provide a higher-resolution image of the zone where the Pollino swarm developed: [lon: 15.8–16.2 (44 km); lat: 39.8–40.05 (21 km); depth: 12 km].

4 METHODS

4.1 Assumption of frequency dependence

The (in)dependence of Q on frequency has been a debated question for decades and is a central assumption for any imaging technique using attenuation as attribute (i.e. *attenuation tomography*). When Q is considered independent of frequency (Knopoff 1964), a valid assumption for measuring attenuation, for example, in rock-physics (Tisato & Madonna 2012), the frequency-shift method becomes the ideal technique to image Earth media (Quan & Harris 1997). Still, the complex heterogeneous attenuation of the lithosphere causes simultaneous phenomena which span, among others: (1) the enhancement of high-frequency near-receiver surface waves due to scattering (Campman *et al.* 2005; Gabrielli *et al.* 2020); (2) anisotropic attenuation due to fractures (Chapman 2003); (3) the wave-induced flow acting at frequencies lower than 1 Hz (Pride *et al.* 2004; Müller *et al.* 2010). Most researchers agree that Q measurements are dependent, if not proportional, to frequency, at least at field scale and above 1 Hz (Fedotov & Boldyrev 1969; Rautian & Khalturin 1978; Aki 1980; Chapman 2003; Li & Lu 2010). The following imaging

is thus performed at multiple frequencies. In zones of high resolution, frequency-dependent images can be interpreted in terms of scale-variations in geological structures and tectonic activity (Sato *et al.* 2012).

4.2 The coda normalization equation

Seismic wave amplitudes can be modelled as the convolution of the source, path, site, and instrument functions in the time domain (Del Pezzo *et al.* 2006). The spectral amplitude of direct *S* waves :

$$A_S(f,r) = R_{\theta\phi} S_S(f) r^{-\gamma} I(f) G(f,\Psi) \exp\left(-\frac{\pi f}{Q_S(f) v_S} r\right) \quad (1)$$

where f is the frequency, r is the source-receiver distance, t_c is the coda-wave central lapse time, $R_{\theta\phi}$ is the source radiation pattern (θ and ϕ the azimuth and take-off angle for a source–receiver ray), $S_S(f)$ is the source function, γ the geometrical spreading exponent, $I(f)$ the known instrumental response, $G(f, \Psi)$ is the site amplification factor (with Ψ being the incident angle of the ray at the station), Q_S is the *S*-wave quality factor and v_S the average *S*-wave velocity in the medium (Yoshimoto *et al.* 1993).

At late lapse times, where the diffusion regime is reached, the spectral amplitude of coda waves can be written as

$$A_c(f,t_c) = S_S(f) P(f,t_c) G(f) I(f). \quad (2)$$

The coda amplitude must be independent of the hypocentral distance (Calvet & Margerin 2013): for Pollino, this was proven by previous works (Napolitano *et al.* 2020a; Sketsiou *et al.* 2020). The attenuation of coda waves can then be expressed as (Aki & Chouet 1975):

$$P(f,t_c) \simeq t_c^{-n} \exp\left(-2\pi f Q_c^{-1} t_c\right) \quad (3)$$

In this equation, n is the envelope spectral decay, Q_c is the coda quality factor and $A_c(f, t_c)$ does not include the effect of the source radiation pattern.

Eq. (1) can be divided by Eq. (2) to normalize the energy of the spectral amplitude of direct *S* waves using the spectral amplitude of coda waves:

$$\frac{A_S(f,t_c)}{R_{\theta\phi} A_c(f,t_c)} = r^{-\gamma} \frac{G(f,\Psi)}{G(f)} \exp\left(-\frac{\pi f}{Q_S(f) v_S} r\right) \frac{1}{P(f,t_c)}, \quad (4)$$

where the source function $S_S(f)$ and the instrumental response $I(f)$ contributions disappear. If the length of the direct-wave window is chosen appropriately, the contribution of the source radiation pattern $R_{\theta\phi}$ is negligible (De Siena *et al.* 2009). Since early coda consists of randomly scattered waves, the coherency and the source radiation pattern is eventually lost (Takemura *et al.* 2009). De Siena *et al.* (2010) demonstrate that a coda window of 2 s is sufficient to make the radiation pattern quasi-isotropic in a volcanic caldera. Still, the window length must be carefully chosen at each frequency to avoid near-receiver onset of surface waves (Gabrielli *et al.* 2020).

At fixed frequency band and starting lapse-time for coda windows, $P(f, t_c)$ is assumed to be constant in the standard coda-normalization method (Del Pezzo *et al.* 2006; Sato *et al.* 2012). Taking the logarithm, eq. (4) becomes

$$\ln\left[\frac{A_S(f,t_c)}{A_c(f,t_c)}\right] = \ln\left(r^{-\gamma}\right) + \ln\left[\frac{G(f,\Psi)}{G(f)}\right] - \frac{\pi f}{Q_S(f) v_S} r - \ln P(f,t_c). \quad (5)$$

By pre-computing $G(f, \Psi)$ over many earthquakes we remove its dependency on the incident angle Ψ. Finally, dividing by πf, the coda-normalization equation is defined as

$$\frac{1}{\pi f} \ln\left[\frac{A_S(f,t_c)}{A_c(f,t_c)}\right] = -Q_S^{-1} v_S^{-1} r - \gamma \left[\frac{\ln(r)}{\pi f}\right] + K_c(f), \quad (6)$$

where $K_c(f) = \frac{\ln P(f,t_c)}{\pi f}$. Yoshimoto *et al.* (1993) demonstrated that earthquakes within a small magnitude range show the same spectral shape for *P* and *S* waves. Hence, we can write

$$A_c(f,t_c) \propto S_S(f) \propto S_P(t) \quad (7)$$

and that Eq. (6) can be used for coda normalization using *P*-wave velocities (v_P):

$$\frac{1}{\pi f} \ln\left[\frac{A_P(f,t_c)}{A_c(f,t_c)}\right] = -Q_P^{-1} v_P^{-1} r - \gamma \left[\frac{\ln(r)}{\pi f}\right] + K_c(f). \quad (8)$$

Both Eqs (6) and (8) are forward models that can be used in tomography to solve for quality factor variations (Del Pezzo *et al.* 2006; De Siena *et al.* 2010, 2014b). In the following, these forward models are used by MuRAT (Del Pezzo *et al.* 2006; De Siena *et al.* 2014a) in order to map Q at Pollino. The new version, currently integrated in MuRAT2.0 (*https://github.com/LucaDeSiena/MuRAT*), pre-computes spatially varying coda attenuation (Sketsiou *et al.* 2020) and uses it to remove one of the unknowns ($K_c(f)$) from Eqs (6) and (8).

4.3 Tomographic procedure

We follow the methodology developed by Del Pezzo *et al.* (2006) and implemented computationally by De Siena *et al.* (2014a). This methodology uses Eqs (6) and (8) to obtain a tomographic forward model. From the linear regression of Eqs (6) and (8), the average inverse total quality factor is $Q_{P,S}^{-1}$ (where the subscripts refer to either *P*- or *S*-wave amplitudes), the geometrical spreading (γ) and K_c (which is assumed to be *constant* for a fixed frequency band and lapse time) are obtained. As explained before, the only unknown in K_c is the average coda quality factor Q_c (Eq. 3), which is measured experimentally for each source-receiver pair.

This pre-calculation allows to define a new data vector (d_k) for each source-station path (k):

$$d_{P,S}^k = \frac{1}{\pi f} \ln\left[\frac{A_{P,S}^k(f,t_c)}{A_c^k(f,t_c)}\right] - K_c(f,t_c) + \frac{\gamma}{\pi f} \ln(r) + Q_{P,S}^{-1} v_{P,S}^{-1}. \quad (9)$$

The area under study is divided into a grid of M equally spaced nodes and the forward model is derived from Eqs (6) and (8) using the new data vector and defining the inversion matrix $G_{P,S}^{kB}$:

$$d_{P,S}^k = -\sum_{B=1}^{M} l_{P,S}^{kB} s_{P,S}^{B} \left[\delta(Q_{P,S}^B)^{-1}\right] = \sum_{B=1}^{M} G_{P,S}^{kB} \left[\delta(Q_{P,S}^B)^{-1}\right], \quad (10)$$

where k refers to the source-station path, B indicates the Bth of the M blocks that the kth ray crosses, s_B is the slowness of segment of length l_{kB} crossing the Bth block, and $\delta(Q_{P,S}^B)^{-1}$ are the variations from $Q_{P,S}^{-1}$ in each block. Eq. (10) is solved using a zero-order Tikhonov regularization. The damping parameter can be chosen from the corresponding L-curve (Aster *et al.* 2013). The total quality factor in each block is obtained as Q_B^{-1}:

$$(Q_{P,S}^B)^{-1} = (Q_{P,S})^{-1} + \delta(Q_{P,S}^B)^{-1}. \quad (11)$$

5 RESULTS

5.1 Average direct and coda attenuation values and dependence on frequency

We start with reporting the results obtained using Data set 1 (see Sketsiou *et al.* (2020) for details). The dependence of $\ln Q_P^{-1}$ on the

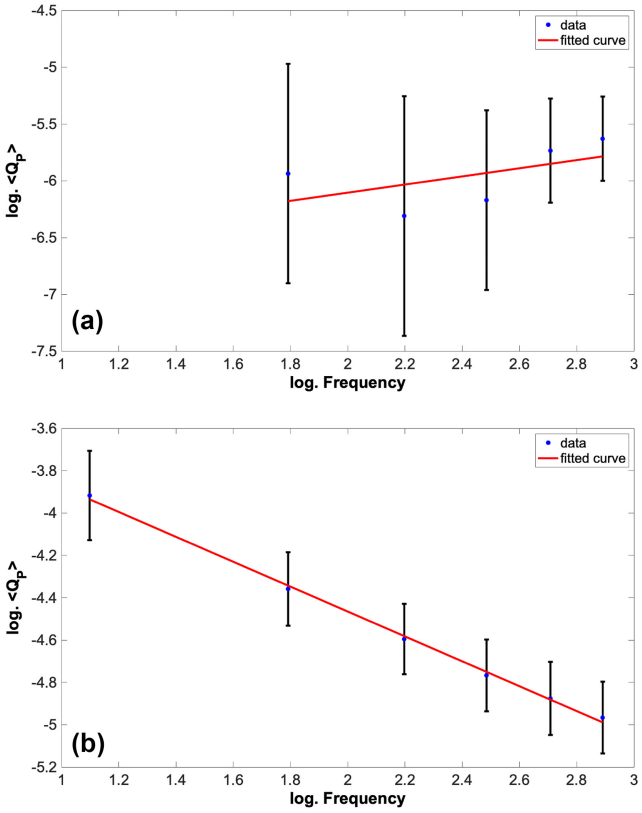

Figure 2. Dependence of the logarithm of the average Q_P^{-1} value in the Pollino area on the logarithm of frequency. Panel (a) shows the results of Data set 1 between 6 and 18 Hz, with their associated error values. Panel (b) shows the results of Data set 2 between 3-18 Hz with their associated error values. The points were fitted using the linearized form of the equation $Q_P^{-1} = Q_0^{-1} \cdot f^{-\eta}$, from which we estimated Q_0^{-1} and η for each data set using linear regression.

Table 1. Best set of input parameters. t_c and L_W are the starting lapse-time and length of the coda window, respectively and L_P is the length of the window for the body wave analysis. The window for the analysis of the body waves starts with the *P*-wave onset, and is chosen taking into account the $t_S - t_P$ of the waveforms with the shortest epicentral distance.

$t_c(s)$	$L_W(s)$	$L_P(s)$
15	12	0.8

logarithm of frequency is shown in Fig. 2(a). The points were fitted by taking the logarithm of an equation of the form $Q_P^{-1} = Q_0^{-1} \cdot f^{-\eta}$ (Petrosino *et al.* 2008). Several parameters affecting the results such as the coda window onset t_c and length L_w, length of the *P*-wave window L_P and the envelope spectral decay n have been tested (Havskov *et al.* 2016). The best set of these parameters are shown in Table 1. The values of Q_P and γ obtained using Eq. (9) for frequencies between 3-18 Hz are shown in Table 2. The resulting equation is $Q_P^{-1} = (0.0011 \pm 0.0008) f^{(0.36 \pm 0.32)}$. The *p*-value of the regression model, which tests whether this model fits significantly better than a degenerate model consisting of only a constant term, is equal to 0.343 which is higher than 0.05, meaning that the aforementioned linear model does not adequately represent the data. Additionally, we modelled the dependence of Q_c^{-1} on frequency. The points were fitted with a power law as in the case of Q_P^{-1}, resulting in the relationship $Q_c^{-1} = (0.0057 \pm 0.0006) f^{(-0.55 \pm 0.05)}$.

Table 2. Q_P^{-1} and geometrical spreading γ measurements with their associated errors σ_{Q_P} and σ_γ (one standard deviation) obtained from the linear regression at different frequency bands using the best set of parameters, shown in Table 1.

f (Hz)	$Q_P^{-1} \pm \sigma_{Q_P}$	$\gamma \pm \sigma_\gamma$
3	-0.0051 ± 0.0048	0.890 ± 0.106
6	0.0026 ± 0.0026	0.827 ± 0.112
9	0.0018 ± 0.0019	0.993 ± 0.126
12	0.0021 ± 0.0016	1.092 ± 0.139
15	0.0032 ± 0.0015	0.999 ± 0.153
18	0.0036 ± 0.0013	0.908 ± 0.163

$Q_P^{-1} = Q_0^{-1} f^{-\eta}$Using Data set 2 (Section 3), we calculated the same dependence of Q_P^{-1} on frequency. This data set spans a depth range of just 12 km, half of Data set 1, and are constrained around the source region. With the same set of input parameters as described for Data set 1 (Table 1), the resulting relationship is $Q_P^{-1} = (0.0373 \pm 0.0011) f^{(-0.59 \pm 0.01)}$, showing the expected higher attenuation and frequency dependence. The *p*-value of the regression model is equal to 1.61×10^{-6}, which is significantly lower than 0.05, meaning that the linear model represents the data well. However, the dependence of Q_c^{-1} on frequency results in the relationship $Q_c^{-1} = (0.0057 \pm 0.0006) f^{(-0.55 \pm 0.05)}$, which is identical to Data set 1. This is a strong indication that coda waves behave homogeneously in space regardless of the size of our study area at the chosen lapse times. The Q_0^{-1} and η values obtained are characteristic of stable continental crust (Data set 1) and high-seismicity zones (Data set 2), respectively (Sato *et al.* 2012).

5.2 Frequency-dependent tomographic results

We obtain several 3-D models of the Pollino fault network in different frequency bands and interpret them in terms of both resolved features and scale of the heterogeneity. We consider horizontal slices taken at 2.5 km, 7.5 km and 12.5 km in the three frequency bands (Figs 3(a)–(i)) as well as S–N, W–E and NW–SE vertical profiles crossing the area of the Pollino swarm (Supporting Information Fig. S1).

Given the velocities we used (Barberi *et al.* 2004) and the depths sampled by the earthquakes, we expect to resolve structures of the order of 10 km^3 across the medium at 3 Hz (Fig. 4, top row). The only resolved anomaly at a depth of 2.5 km at all frequencies is a low-attenuation pattern located just above the volume where the last Pollino swarm occurred (Figs 3(a)–(c)). At 7.5 km, most of the volumes west of 16.3° longitude and centred at 7.5 km are resolved (Fig. 4, middle row). Here, high attenuation anomalies trending NW-SE (Fig. 3(d)) appear across the northern fault network, following historical seismicity (Fig. 1). The area of the Pollino swarm, centred at this depth around [16.0 lon, 39.9 lat], has average attenuation characteristics. At a depth of 12.5 km, the resolved region is between 15.9–16.3 lon and 39.8–40.04 lat (Figs 3(g), S1). Two high attenuation anomalies are located NW and SE of the shallower epicentral area of the Pollino swarm (Fig. 3(g)), respectively. The NW high-attenuation anomaly is at the borderline of our resolving power (Fig. 4, bottom row) and possibly a ghost. The resolved SE high-attenuation anomaly corresponds to the oldest historical seismicity recorded in the area (Tertulliani & Cucci 2014).

A NW–SE vertical cross-section (Supporting Information Fig. S1) shows that the low-attenuation volume topping the epicentral area extends from the surface down to a depth of 5 km above the Pollino swarm. The N–S and W–E profiles, taken at 16.01 lon

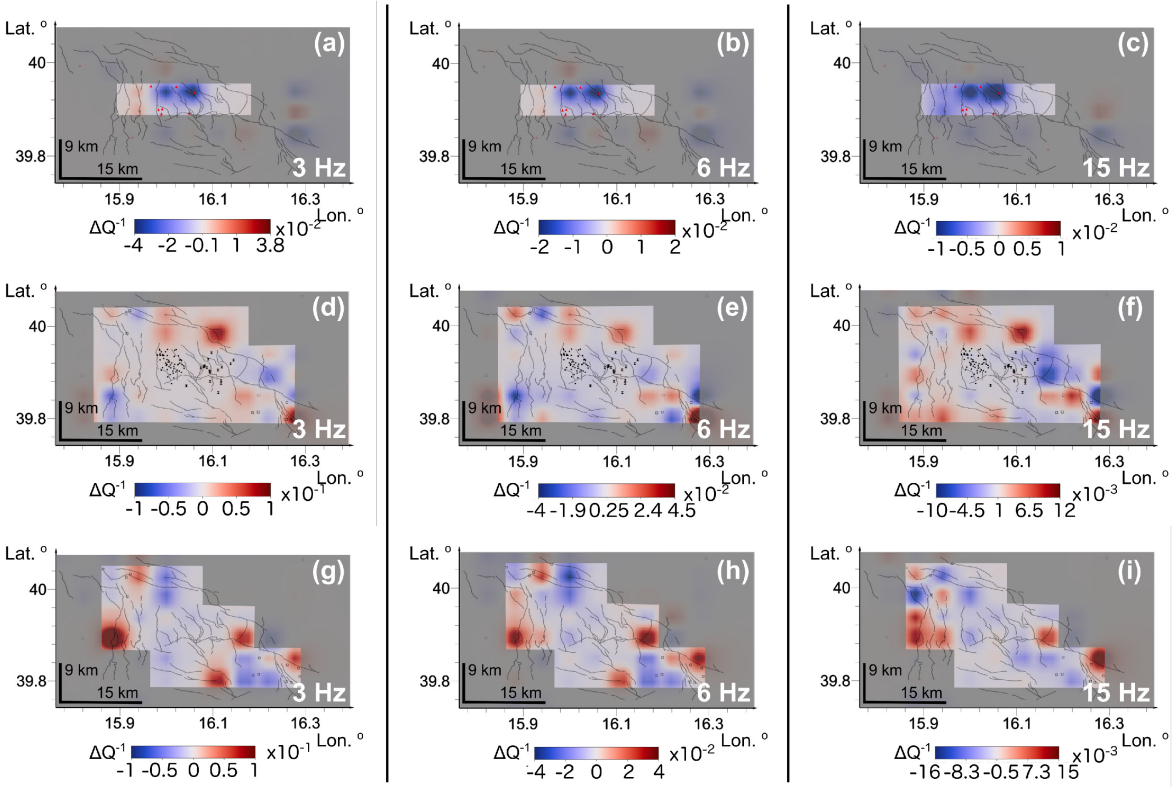

Figure 3. Maps of ΔQ^{-1}, at three different depths and three central frequencies (3, 6 and 15 Hz) using Data set 1. Top row panels (a)–(c) are at 2.5 km depth, middle row panels (d)–(f) are at 7.5 km depth and bottom row panels (g)–(i) are at 12.5 km depth. The central frequency is shown at the bottom right corner of each panel. The grey areas are beyond our resolution power and they have been masked for simplification. The black lines on the panels represent the main faults in the area, adapted from Brozzetti *et al.* (2017). The red triangles on the top row panels represent the seismic stations in the area. In the rest of the panels, the black circle markers represent the events of cluster 1 events, the hourglass markers represent the events of cluster 2 events and the open square markers represent the rest of the seismicity in the area. A scale bar is shown on the bottom left corner of each plot.

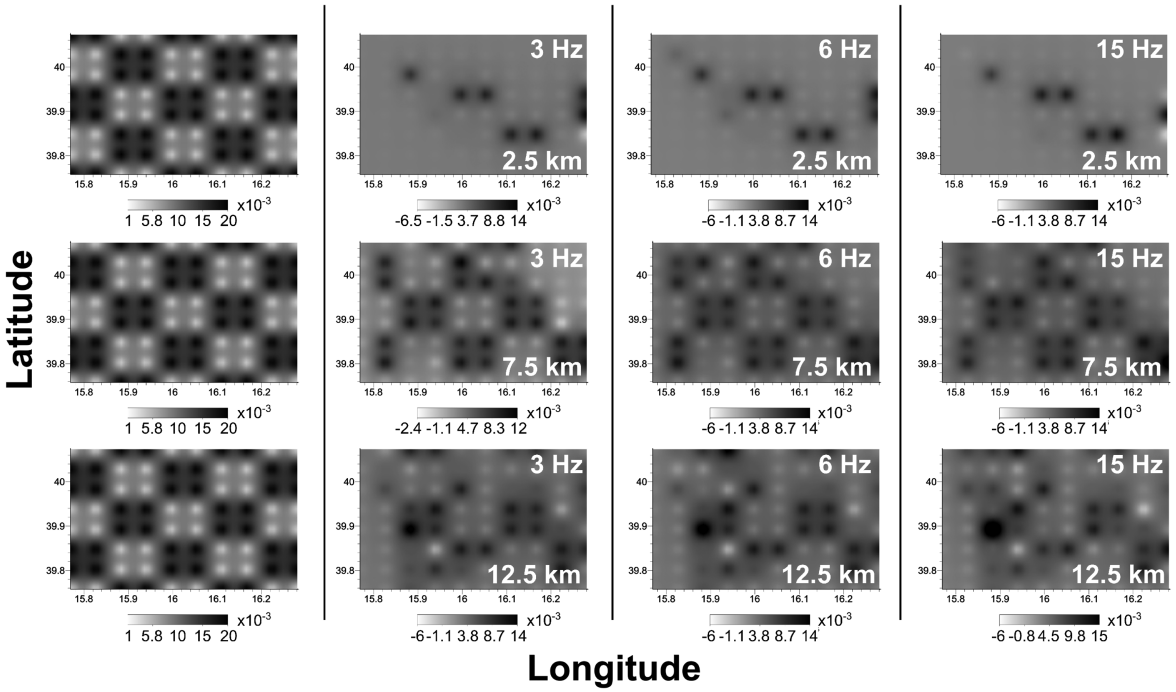

Figure 4. Results of the checkerboard tests for the three depth slices at 2.5 (top row panels), 7.5 (middle row panels) and 12.5 km (bottom row) depths, at three central frequencies: 3 Hz (second column), 6 Hz (third column) and 15 Hz (last column). The first column shows the checkerboard inputs.

and 39.92 lat, respectively (Supporting Information Fig. S1) show that this medium-to-low attenuation volume characterizes the whole southern portion of the study area. While the rupture zone for the M5 Pollino earthquake is sandwiched at the top of the two deeper high-attenuation anomalies in the NW and SE, only the SE anomaly (1) is resolved and (2) is related to historical seismicity. The only resolved high-attenuation anomaly at the average depth of the swarm (7.5 km) is north of it (Figs 3(d)–(f) and Supporting Information Figs S1(d)–(f)).

The 6 Hz model confirms the broadest features visible in the 3 Hz maps (Figs 3(b),(e),(h)):

(i) a wide low-attenuation volume extending above and to the south of the Pollino hypocentral area down to 5 km;
(ii) the NW–SE trend of high attenuation volumes centred at a depth of 7.5 km and following historical seismicity;
(iii) two high-attenuation volumes sitting just below the hypocentral area (12.5 km depth), although again the northern anomalies are unresolved;
(iv) the high-attenuation volume at 7.5 km depth, located just north of the hypocentral area showing average attenuation characteristics.

The 15 Hz maps provide a more resolved reconstruction of all the high- and low-attenuation anomalies listed above (Figs 3(c),(f),(i)). However, the high-attenuation anomaly north of the hypocentral area at 7.5 km now extends southwards along the NS-trending faults west of the swarm area.

The resolution tests at 2.5 km depth show that the only resolved area is directly above the swarm for Data set 1 (Fig. 4, top row). At 7.5 km, the majority of our study area is resolved, up to 16.3° lon using Data set 1 (Fig. 4, middle row). Using Data set 2, the majority of the area between 15.88° and 16.14° lon is resolved at this depth (Fig. 5). At 12.5 km depth, the resolved area for Data set 1 is between 15.9-16.3° lon and 39.8-40.04° lat (Fig. 4, bottom row).

For Data set 2 the resolution is limited both above and below 7.5 km due to the lower ray-crossing (Figs 5(b),(e),(h)). Regardless, they provide more details in the area of the seismic sequence than Data set 1 around a depth of 7.5 km (Figs 5(b),(e)). The high-attenuation anomaly previously comprising the Mercure basin now extends across the western side of the cluster 1 events and stops in the NW and W due to a sharp low-attenuation interface, at the boundary of our lateral resolving power (Figs 5(c),(f),(i)). The low-to-average attenuation anomaly previously characterizing the entire seismic sequence now comprises only the eastern part of the cluster 1 events, as well as the aseismic zone between clusters 1 and 2.

6 DISCUSSION

Fig. 6 is a simplified sketch of our tomographic model and includes geophysical and geological results used in the following interpretation. We primarily refer to this sketch while mentioning the tomographic sections when discussing resolution and reliability.

6.1 Frequency dependence of seismic attenuation measurements

Using Data set 1, there appears to be no dependence of Q_P^{-1} on frequency (Fig. 2 (a)). Considering the error on each value, we see that the trend is approximately constant, showing nearly no dependency on frequency. The reduction of the study area with Data set 2 led to focusing on the fault networks and, as a result, the Q_P^{-1} dependence on frequency is significant. The Q_0 and η values obtained are indicative of tectonically active areas (Padhy 2005; Sato *et al.* 2012). The Q_{c0}^{-1} and η values obtained using Data sets 1 and 2 are the same: they indicate that coda waves behave similarly regardless of the size of our study area and they are characteristic of continental areas with high seismicity (Sato *et al.* 2012).

6.2 Low-permeability shallow volumes topping lateral seismic migration

The low-attenuation volume topping the hypocentral area of the cluster 1 events (depth of 2.5 km) corresponds to a relative absence of extended faulting and, consequently, lack of historical and more recent seismicity (Fig. 6(a); Tertulliani & Cucci 2014; Ferranti *et al.* 2017). This volume seems able to stop the vertical rupture of the western fault during the Pollino sequence. As fluids are the likely cause of swarms and aseismic transients (Passarelli *et al.* 2015; Cheloni *et al.* 2017; Napolitano *et al.* 2020a), the volume could mark semi-impermeable formations. The presence of such an impermeable layer at 4.5–5 km depth and lat >39.92° is supported by the highly detailed relative location of clusters having similar waveforms, obtained by Napolitano *et al.* (2020b) and shown in its figs. 10 and 11. The hypocentres migrated horizontally (between 4.5 and 6 km depth) from the middle of the fault network towards North between Nov. 2011 and Feb. 2012, just below the interpreted impermeable formation. The re-located hypocentres started propagating vertically between Sept. 2012 and June 2013, only after the seismicity migrated towards the South over the boundary of the low-attenuation anomaly (lat <39.92°). The results of these two independent analyses obtained using different data sets, consistently point to a mechanism of lateral fluid migration and, possibly, excess of pore fluids (Passarelli *et al.* 2015), as the cause of the Pollino seismic sequence. The distribution of deep-sourced springs shows that these deep-sourced fluids find their way to surface along the SW boundary of the formations (Gaglioti *et al.* 2019), in spatial relation with the main aseismic transient, synchronous to the swarm (Cheloni *et al.* 2017) (Fig. 6).

At these depths, impermeable formations would correspond mostly to the transition from the shallower ductile-behaving Apennines imbricate wedge and the brittle Apulia sedimentary crust (Ferranti *et al.* 2017). According to Brozzetti *et al.* (2017), the location comprises a part of the Mercure basin, a part of a Liguride unit and a part of the Apennine platform western unit. The first ∼ 2 km layer of sediments in the area (limestones and dolomites) have thus likely high permeability.

6.3 Deep fluid reservoirs and low-attenuation, low-seismicity gap between the two clusters

All the higher resolution maps (Fig. 5) show that a wide high-attenuation volume develops at a depth of 7.5 km across the Mercure basin, and comprises the western and central part of the cluster 1 events (Figs 5 and 6). Constrained in the north, west (Lauria) and east (Pollino Range) by the low-attenuation eastern unit of the Apennine Platform (Knott 1987; Giaccio *et al.* 2014; Brozzetti *et al.* 2017; Fig. 6), the high-attenuation volumes are likely representing the seismic signature of a deep fluid reservoir in the area ('Mercure reservoir'). These deep fluids find their way to the surface across the boundary between the reservoir and the Lauria mountains, the

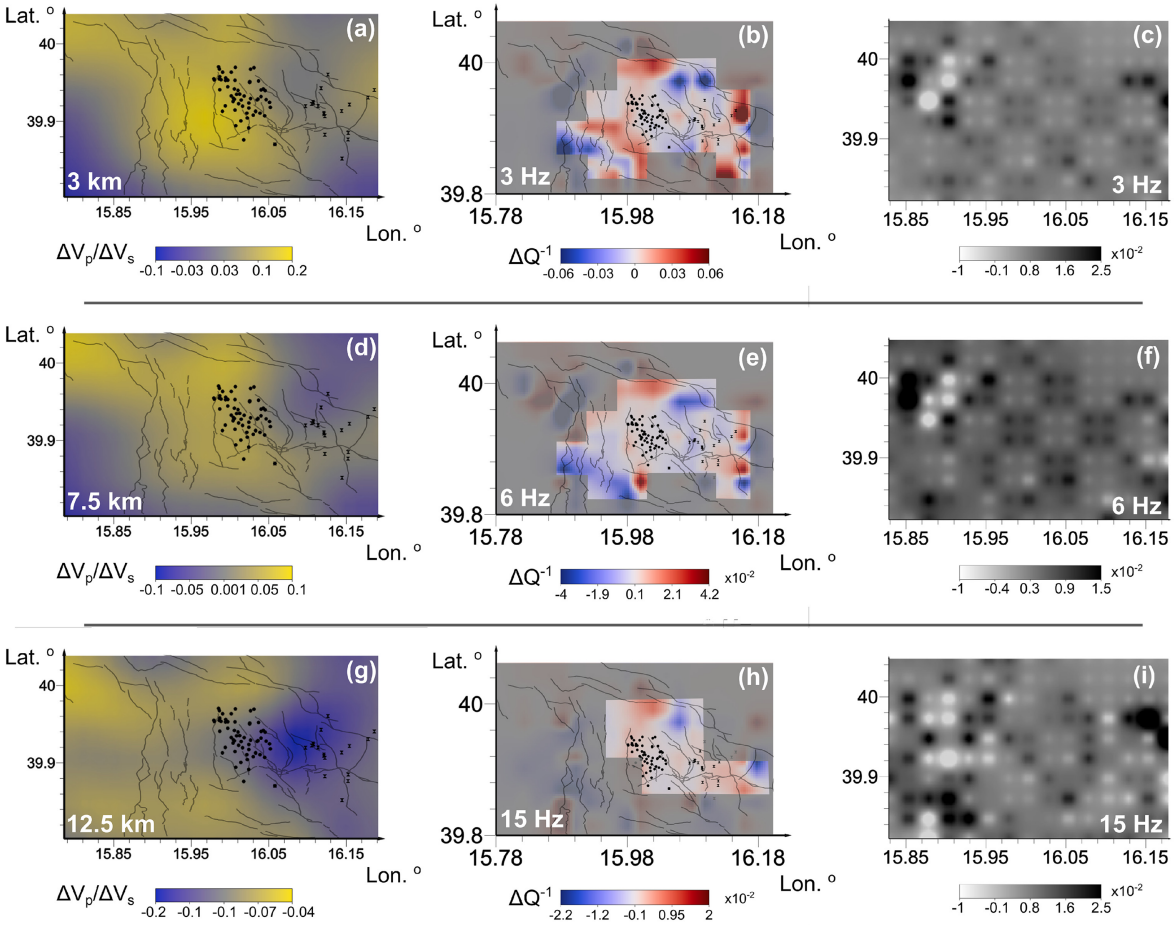

Figure 5. Maps of $\Delta V_P/\Delta V_S$ velocity variations (left column) at 3 km, 7.5 km and 12.5 km depth and ΔQ^{-1} at 7.5 km depth (middle column) at three central frequencies (3, 6 and 15 Hz) using Data set 2, with the associated checkerboard tests for attenuation (right column panels). The central frequency is shown at the bottom left corner on the Q^{-1} maps and at the bottom right corner of the checkerboards. The grey areas on the Q^{-1} maps are beyond our resolution power and they have been masked for simplification. The velocity model was adapted from Totaro *et al.* (2014).

primary region of deep-sourced springs in the study area (Margiotta *et al.* 2012; Canora *et al.* 2019).

A low-attenuation volume develops inside the low-seismicity gap between cluster 1 and cluster 2 events (Figs 5 and 6(b)). It separates the Mercure reservoir from a second high-attenuation anomaly, east of the cluster 2 events and underlying the Castrovillari basin. This high attenuation volume dips towards SE, below 10 km (Fig. 6(b)). The low-attenuation gap underlies (likely young) small-scale cross-faulting (Brozzetti *et al.* 2017) and comprises patches of high attenuation that increase in size at higher frequencies. There is no clear indication of consistent high-attenuation pathways between the Mercure and Castrovillari reservoirs, and these patches are below our resolution power. However, the attenuation values in this volume are higher than those in the surrounding regions (parts of the eastern units of the Appenine platform) (Fig. 6). These observations are hardly explained by the presence of a barrier for fluid migration similar to that inferred under the Lauria Mountains (Fig. 6). They better agree with the hypothesis that the volume comprises a system of asperities (Passarelli *et al.* 2015) that can break in the low-attenuation matrix.

The attenuation structure obtained using Data set 2 was compared with the velocity model of Totaro *et al.* (2014), which is different from the 1-D velocity model of Barberi *et al.* (2004) we used for our tomographic procedure. In their paper, Totaro *et al.* (2014) studied the crustal V_P, V_S and V_P/V_S structure of the southern Apennine–Calabrian arc border between 3 km and 30 km. For our study, the original model was interpolated between 3 km and 12.5 km and cross-sections at 3 km, 7.5 km and 12.5 km were plotted for our area of interest (Figs 5 and S3). In Fig. 5 positive and negative variations of attenuation are spatially correlated with positive and negative variations of V_P/V_S. The low V_P/V_S and attenuation support the interpretation of the low-seismicity gap as a poorly permeable system that slows down fluid migration.

The impermeable formations capping the cluster 1 events area and this deep low-attenuation volume depict the ideal setting for the development of transient slip events due to fluid redistribution and migration within the Mercure reservoir and adjacent faults (Passarelli *et al.* 2015). The aseismic transient identified during the seismic sequence by Cheloni *et al.* (2017) is located just under the impermeable formations. The transient develops NW across the reservoir, consistent with the transtensional stress field acting in the southern part of the Mercure Basin, associated with NNW–SSE normal faulting (Passarelli *et al.* 2015).

6.4 Fluid sources and earthquake-inducing fluid migration

Our model depicts a closed reservoir system lacking high-attenuation fluid sources that could create pressure directly below

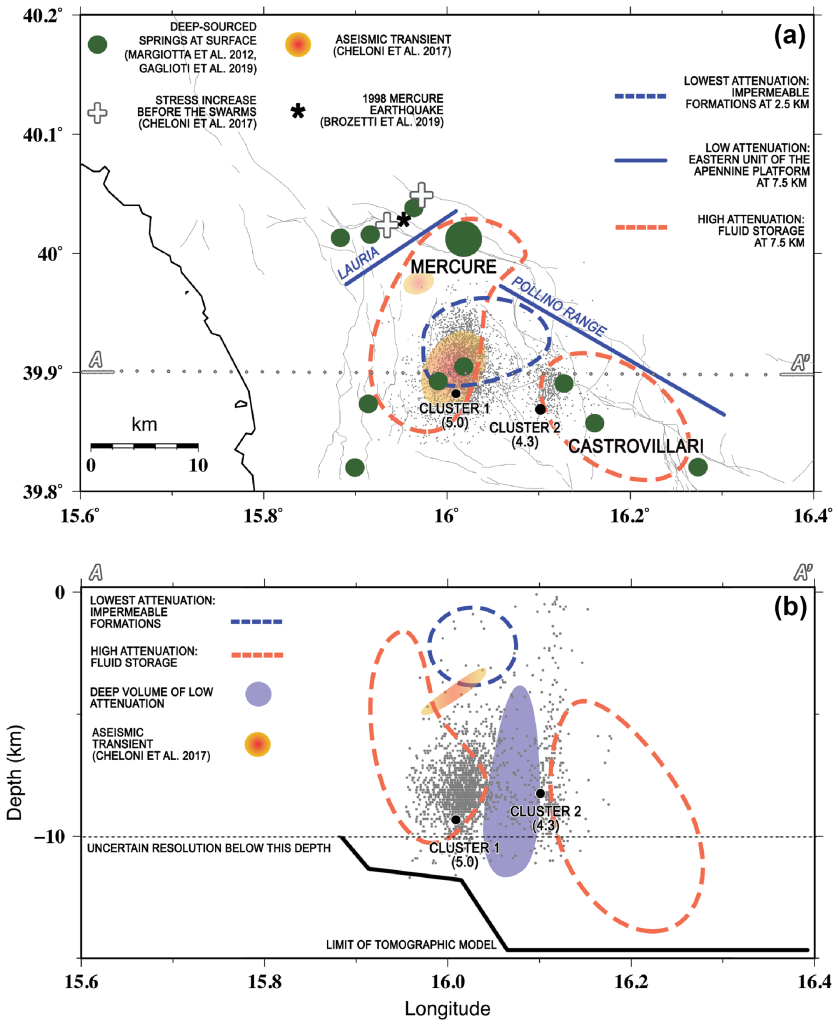

Figure 6. Schematic interpretation of the attenuation model, as described in the text, illustrating the main findings. In panel (a), we show a horizontal section of the region with the small grey dots representing the seismicity, and including the location of the 1998 Mercure earthquake (Brozzetti *et al.* 2009). The dashed orange shapes represent high attenuation regions and the dashed blue shapes represent shallow low-attenuation volumes. The solid blue lines represent low attenuation regions related to mountain platforms. Three areas of increased stress before the swarm are marked with a white cross as well as two areas of aseismic transient. Surface springs with deep sources are marked with green circles. Panel (b) is an E–W cross section at 39.9° latitude. The seismicity of the region at depth, the low- and high-attenuation volumes and the aseismic transient are shown, as described before for panel (a). We also show the deep low-seismicity and low-attenuation volume in light purple. The dashed black line marks the borderline of our resolution and the solid black line marks the limit of the tomographic model.

the cluster 1 events (Fig. 3). Our models lose resolution at depths below 10 km, especially when using Data set 2 (Fig. 5) and are clearly more affected by the interpolation of the broader velocity model (Barberi *et al.* 2004), necessary to obtain high-resolution attenuation maps. We observe deep anomalies (12.5 km) west of the seismic events, corresponding to old extended NS-trending faults (Brozzetti *et al.* 2017; Figs 3(g)–(i)). These anomalies are unresolved and, given their aseismicity (both recent and historical), they are likely ghosts produced, for example, by the shallower Mercure reservoir. Despite the uncertainties, at least at the wider scale (Data set 1—Fig. 3), we are able to resolve a single deep high-attenuation volume that shows the extension to depth of the Castrovillari reservoir, SE of the fault networks (Figs 3 and 6).

The absence of high-attenuation volumes sourcing fluids just below the cluster 1 events (Figs 3(d)–(i) and 5) is expected given the structural characteristics of the area (Brozzetti *et al.* 2017; Ferranti *et al.* 2017) and the evidence of historical (Napolitano *et al.* 2020a) and recent (Passarelli *et al.* 2015; Napolitano *et al.* 2020b) lateral fluid migration. Historical earthquakes correlate with a general shift of fluid-related, high-absorption anomalies from the Castrovillari basin towards the NW, stopping at the foot of the Lauria mountains (Napolitano *et al.* 2020a). Even today, the deep volumes below the Castrovillari basin seem the most likely source of deep fluids. Here, at depths between 9 km and 14 km, Ferranti *et al.* (2017) speculate the existence of the ductile Verrucano (s. l.) layer, a siliciclastic and lower-velocity layer that rises above its average depth in the eastern part of our model. Similar ductile characteristics are detected as high-attenuation anomalies when mapping volcanoes with seismic attenuation (De Siena *et al.* 2017), thus they could affect imaging of the deeper volumes.

The trace of the Mercure reservoir at 7.5 km depth is close to the hypocentral location of the Mercure basin seismic sequence in 1998 (Brozzetti *et al.* 2009) (see main shock in Fig. 6). Our tests (Fig. 4 and Supporting Information Fig. S2) show that the interface

under the Lauria mountain is a reliably reconstructed barrier for NW propagation, where stress accumulates at the end of aseismic transients (Cheloni *et al.* 2017; Fig. 6). This barrier is the same acting on historical seismicity, hindering its general SE-to-NW migration (Napolitano *et al.* 2020a). The evolution of the Pollino swarm sequence, with transient aseismic and seismic events alternating west and east of the low-attenuation low-seismicity structure, suggests a mechanism of fluid migration within sealed structures developing mostly across the strike of late Pleistocene-Holocene faults (Brozzetti *et al.* 2017). The stress changes caused by seismic activity and the increased fault zone permeability due to fracture opening leads to fluid re-distribution through seismic and aseismic slip (Passarelli *et al.* 2015; Cheloni *et al.* 2017). The fluid distribution returns to equilibrium when the seismic activity fades out. The recovered attenuation structure represents a temporal average of the short- and long-term processes that developed in the area.

The Mercure reservoir is likely fluid-saturated so any fluid input within the reservoir increases pore fluid pressure in fluid-filled cracks around faults (Amoroso *et al.* 2014; Passarelli *et al.* 2015). The highest-magnitude seismicity consistently develops at the interface of the low-attenuation volume separating the cluster 1 and cluster 2 events, in the region of strongest short-scale cross faulting. We infer that this volume is a major structural control for the dynamics of this and following seismic sequences; if our inference about fault patches is correct, the volume could fail seismically in the future. Additional geophysical studies which integrate a range of interdisciplinary methods, a more detailed velocity model of the area, and broader seismic data sets better encompassing the study area are needed to investigate the proposed hypotheses further.

7 CONCLUSIONS

High seismic-attenuation anomalies are a reliable marker for fluid accumulation and propagation in the lithosphere. In a setting where fluid migration and changes in pore pressure are expected as the main trigger for aseismic transient and seismicity, our results offer a 3-D structural framework to interpret where fluids come from and how they interact with complex tectonics to nucleate swarms and feed springs at the surface. This fluid accumulation (depth of 7.5 km) underlies the two primary sedimentary basins of the study area, Mercure and Castrovillari.

The structures and dynamics affecting these two reservoirs appear different, with deeper high-attenuation anomalies (12.5 km) sourcing fluids only under the Castrovillari basin. There is no high-attenuation volume directly below the cluster 1 events. The low-attenuation volume directly above the area of the cluster 1 events correlates with the presence of impermeable formations possibly enhanced by changes in fault mechanisms. This low-attenuation volume as well as those corresponding to the ductile low-V_P eastern unit of the Apennine Platform are contoured by deep-sourced springs and likely control the spring feeding mechanisms. Seismicity before the swarm develops mostly horizontally and below the impermeable formations, supporting an interpretation in terms of lateral fluid migration. The primary deep source region for these fluids is located under the Castrovillari basin, with fluid migration possibly developing from SE (Castrovillari basin) to the NW (Mercure basin). This trend corresponds to the fluid/stress migration derived from historical seismicity and stops under the Lauria mountains due to a sharp high-to-low attenuation contrast. However, along this trend, the two clusters of the Pollino sequence develop on either side of a deep low-attenuation volume, showing no direct high-attenuation pathways for fluid migration. Our results suggest no barrier between reservoirs. More likely, delayed lateral stress exchange accommodates on small fault patches that allow fluid propagation and could break in the future.

ACKNOWLEDGEMENTS

This work was undertaken as part of the Natural Environment Research Council (NERC) Centre for Doctoral Training (CDT) in Oil and Gas [grant number NEM00578X/1]. It is sponsored by University of Aberdeen whose support is gratefully acknowledged. We thank EIDA Data Archives for data archiving and the Universitá della Calabria for providing the data set for this study. We thank Dr Cristina Totaro for providing the velocity model used for comparison with our results. We would also like to thank two anonymous reviewers whose constructive feedback greatly improved the original manuscript.

DATA AVAILABILITY

Waveforms of temporary stations used in this paper were provided by Universitá della Calabria and are available upon request. Seismograms recorded by INGV seismic stations (CUC, MTSN, MGR, SALB) were extracted by EIDA Data Archives at http://www.webdc.eu/webdc3/ (last access August 2017). Figures of this paper were produced using Voxler (Golden Software LLC, www.goldensoftware.com), Inkscape for MacOS X (version 1.0beta) and Adobe® Photoshop®.

REFERENCES

Aki, K., 1980. Attenuation of shear-waves in the lithosphere for frequencies from 0.05 to 25 Hz, *Phys. Earth planet. Inter.,* **21**(1), 50–60.

Aki, K. & Chouet, B., 1975. Origin of coda waves: source, attenuation, and scattering effects, *J. geophys. Res.,* **80**(23), 3322–3342.

Akinci, A. & Eyidoğan, H., 1996. Frequency-dependent attenuation of S and coda waves in Erzincan region (Turkey), *Phys. Earth planet. Inter.,* **97**(1–4), 109–119.

Amoroso, O., Ascione, A., Mazzoli, S., Virieux, J. & Zollo, A., 2014. Seismic imaging of a fluid storage in the actively extending Apennine mountain belt, southern Italy, *Geophys. Res. Lett.,* **41**(11), 3802–3809.

Aster, R., Borchers, B. & Thurber, C., 2013, *Parameter Estimation and Inverse Problems,* 2nd edn, Elsevier Inc.

Barberi, G., Cosentino, M., Gervasi, A., Guerra, I., Neri, G. & Orecchio, B., 2004. Crustal seismic tomography in the Calabrian Arc region, south Italy, *Phys. Earth planet. Inter.,* **147**(4), 297–314.

Bindi, D., Parolai, S., Grosser, H., Milkereit, C. & Zunbul, S., 2006. Cumulative attenuation along source-to-receiver paths in northwestern Turkey, *Bull. seism. Soc. Am.,* **96**(1), 188–199.

Brozzetti, F., Lavecchia, G., Mancini, G., Milana, G. & Cardinali, M., 2009. Analysis of the 9 September 1998 Mw 5.6 Mercure earthquake sequence (Southern Apennines, Italy): a multidisciplinary approach, *Tectonophysics,* **476**(1–2), 210–225.

Brozzetti, F., Cirillo, D., de Nardis, R., Cardinali, M., Lavecchia, G., Orecchio, B., Presti, D. & Totaro, C., 2017. Newly identified active faults in the Pollino seismic gap, southern Italy, and their seismotectonic significance, *J. Struct. Geol.,* **94,** 13–31.

Calvet, M. & Margerin, L., 2013. Lapse-time dependence of coda Q: Anisotropic multiple-scattering models and application to the Pyrenees, *Bull. seism. Soc. Am.,* **103**(3), 1993–2010.

Campman, X. H., Van Wijk, K., Scales, J.A. & Herman, G.C., 2005. Imaging and suppressing near-receiver scattered surface waves, *Geophysics,* **70**(2), V21–V29.

Canora, F., Rizzo, G., Panariello, S. & Sdao, F., 2019. Hydrogeology and hydrogeochemistry of the Lauria mountains northern sector groundwater resources (Basilicata, Italy), *Geofluids,* **2019,** doi:10.1155/2019/7039165.

Chapman, M., 2003. Frequency-dependent anisotropy due to meso-scale fractures in the presence of equant porosity, *Geophys. Prospect.,* **51**(5), 369–379.

Cheloni, D. *et al.*, 2017. Aseismic transient during the 2010–2014 seismic swarm: evidence for longer recurrence of M 6.5 earthquakes in the Pollino gap (Southern Italy)?, *Sci. Rep.,* **7**(1), 1–10.

Chiarabba, C., Piccinini, D. & De Gori, P., 2009. Velocity and attenuation tomography of the Umbria Marche 1997 fault system:evidence of a fluid-governed seismic sequence, *Tectonophysics,* **476**(1–2), 73–84.

Cormier, V.F., 1982. The effect of attenuation on seismic body waves, *Bull. seism. Soc. Am.,* **72**(6B), S169–S200.

Cormier, V.F., 2011. *Seismic, Viscoelastic Attenuation,* pp. 1279–1290, Springer Netherlands.

De Siena, L., Del Pezzo, E., Bianco, F. & Tramelli, A., 2009. Multiple resolution seismic attenuation imaging at Mt. Vesuvius, *Phys. Earth planet. Inter.,* **173**(1–2), 17–32.

De Siena, L., Del Pezzo, E. & Bianco, F., 2010. Seismic attenuation imaging of Campi Flegrei: evidence of gas reservoirs, hydrothermal basins, and feeding systems, *J. geophys. Res.,* **115**(B9), doi:10.1029/2009JB006938.

De Siena, L., Thomas, C. & Aster, R., 2014a. Multi-scale reasonable attenuation tomography analysis (MuRAT): An imaging algorithm designed for volcanic regions, *J. Volc. Geotherm. Res.,* **277,** 22–35.

De Siena, L., Thomas, C., Waite, G.P., Moran, S.C. & Klemme, S., 2014b. Attenuation and scattering tomography of the deep plumbing system of Mount St. Helens, *J. geophys. Res.,* **119**(11), 8223–8238.

De Siena, L., Chiodini, G., Vilardo, G., Del Pezzo, E., Castellano, M., Colombelli, S., Tisato, N. & Ventura, G., 2017. Source and dynamics of a volcanic caldera unrest: Campi Flegrei, 1983–84, *Sci. Rep.,* **7**(1), 8099, doi:10.1038/s41598-017-08192-7.

Del Pezzo, E., 2008. Seismic wave scattering in volcanoes, *Adv. Geophys.,* **50,** 353–371.

Del Pezzo, E., Bianco, F., De Siena, L. & Zollo, A., 2006. Small scale shallow attenuation structure at Mt. Vesuvius, Italy, *Phys. Earth planet. Inter.,* **157**(3), 257–268.

Fedotov, S. & Boldyrev, S., 1969. Frequency dependence of the body-wave absorption in the crust and the upper mantle of the Kuril Island chain, *Izv. Acad. Sci. USSR Solid Earth,* **11,** 553–562.

Ferranti, L., Milano, G. & Pierro, M., 2017. Insights on the seismotectonics of the western part of northern Calabria (southern Italy) by integrated geological and geophysical data: Coexistence of shallow extensional and deep strike-slip kinematics, *Tectonophysics,* **721,** 372–386.

Frankel, A., McGarr, A., Bicknell, J., Mori, J., Seeber, L. & Cranswick, E., 1990. Attenuation of high-frequency shear waves in the crust: Measurements from New York state, South Africa, and southern California, *J. geophys. Res.,* **95**(B11), 17 441–17 457.

Gabrielli, S., De Siena, L., Napolitano, F. & Del Pezzo, E., 2020. Understanding seismic path biases and magmatic activity at Mount St Helens volcano before its 2004 eruption, *Geophys. J. Int.,* **222**(1), 169–188.

Gaglioti, S., Infusino, E., Caloiero, T., Callegari, G. & Guagliardi, I., 2019. Geochemical characterization of spring waters in the Crati river basin, Calabria (Southern Italy), *Geofluids,* **2019,** doi:10.1155/2019/3850148.

Giaccio, B. *et al.*, 2014. A 560–440 ka tephra record from the Mercure Basin, southern Italy: volcanological and tephrostratigraphic implications, *J. Quat. Sci.,* **29**(3), 232–248.

Havskov, J., Sørensen, M.B., Vales, D., Özyazıcıoğlu, M., Sánchez, G. & Li, B., 2016. Coda Q in different tectonic areas, influence of processing parameters, *Bull. seism. Soc. Am.,* **106**(3), 956–970.

Kanamori, H., 1967. Spectrum of short-period core phases in relation to the attenuation in the mantle, *J. geophys. Res.,* **72**(8), 2181–2186.

Knopoff, L., 1964. Q, *Rev. Geophys.,* **2**(4), 625–660.

Knott, S.D., 1987. The Liguride complex of southern Italy–a Cretaceous to Paleogene accretionary wedge, *Tectonophysics,* **142**(2–4), 217–226.

Li, L. & Lu, J., 2010. Ambiguity between the residual geometrical spreading and scattering attenuation, *Pure appl. Geophys.,* **167**(12), 1579–1580.

Margheriti, L. *et al.*, 2013. Emergenza nell'area del Pollino: le attività della Rete Sismica Mobile, *Rapporti Tecnici INGV*.

Margiotta, S., Mongelli, G., Summa, V., Paternoster, M. & Fiore, S., 2012. Trace element distribution and Cr (VI) speciation in Ca-HCO_3 and Mg-HCO_3 spring waters from the northern sector of the Pollino massif, southern Italy, *J. Geochem. Explor.,* **115,** 1–12.

Matsumoto, S. *et al.*, 2009. High resolution Q- 1 estimation based on extension of coda normalization method and its application to P-wave attenuation structure in the aftershock area of the 2005 West Off Fukuoka Prefecture Earthquake (M 7.0), *Geophys. J. Int.,* **179**(2), 1039–1054.

Mayor, J., Calvet, M., Margerin, L., Vanderhaeghe, O. & Traversa, P., 2016. Crustal structure of the Alps as seen by attenuation tomography, *Earth planet. Sci. Lett.,* **439,** 71–80.

Müller, T.M., Gurevich, B. & Lebedev, M., 2010. Seismic wave attenuation and dispersion resulting from wave-induced flow in porous rocks—a review, *Geophysics,* **75**(5), 75A147–75A164.

Napolitano, F., Gervasi, A., La Rocca, M., Guerra, I. & Scarpa, R., 2018. Site effects in the Pollino region from the HVSR and polarization of seismic noise and earthquakes, *Bull. seism. Soc. Am.,* **108**(1), 309–321.

Napolitano, F., De Siena, L., Gervasi, A., Guerra, I., Scarpa, R. & La Rocca, M., 2020a. Scattering and absorption imaging of a highly fractured fluid-filled seismogenetic volume in a region of slow deformation, *Geosci. Front.,* **11**(3), 989–998.

Napolitano, F., Galluzzo, D., Gervasi, A., Scarpa, R. & La Rocca, M., 2021. Fault imaging at Mt. Pollino (Italy) from relative location of microearthquakes, *Geophys. J. Int.,* **224**(1), 637–648.

Nazemi, N., Pezeshk, S. & Sedaghati, F., 2017. Attenuation of Lg waves in the New Madrid seismic zone of the central United States using the coda normalization method, *Tectonophysics,* **712,** 623–633.

Padhy, S., 2005. A scattering model for seismic attenuation and its global applications, *Phys. Earth planet. Inter.,* **148**(1), 1–12.

Parolai, S., Bindi, D. & Pilz, M., 2015. k0: The role of intrinsic and scattering attenuation, *Bull. seism. Soc. Am.,* **105**(2A), 1049–1052.

Parvez, I.A., Yadav, P. & Nagaraj, K., 2012. Attenuation of P, S and coda waves in the NW-Himalayas, India, *Int. J. Geosci.,* **3**(01), 179–191.

Passarelli, L. *et al.*, 2012. Pollino seismic experiment (2012-2014), doi:10.14470/9N904956.

Passarelli, L. *et al.*, 2015. Aseismic transient driving the swarm-like seismic sequence in the Pollino range, Southern Italy, *Geophys. J. Int.,* **201**(3), 1553–1567.

Petrosino, S., De Siena, L. & Del Pezzo, E., 2008. Recalibration of the magnitude scales at Campi Flegrei, Italy, on the basis of measured path and site and transfer functions, *Bull. seism. Soc. Am.,* **98**(4), 1964–1974.

Pride, S.R., Berryman, J.G. & Harris, J.M., 2004. Seismic attenuation due to wave-induced flow, *J. geophys. Res.,* **109**(B1), doi:10.1029/2003JB002639.

Prudencio, J. & Manga, M., 2019. 3-D seismic attenuation structure of Long Valley caldera: looking for melt bodies in the shallow crust, *Geophys. J. Int.,* **220**(3), 1677–1686.

Prudencio, J., De Siena, L., Ibáñez, J., Del Pezzo, E., García-Yeguas, A. & Díaz-Moreno, A., 2015a. The 3D attenuation structure of deception Island (Antarctica), *Surv. Geophys.,* **36**(3), 371–390.

Prudencio, J., Ibáñez, J., Del Pezzo, E., Martí, J., García-Yeguas, A. & De Siena, L., 2015b. 3D attenuation tomography of the volcanic island of Tenerife (Canary Islands), *Surv. Geophys.,* **36**(5), 693–716.

Quan, Y. & Harris, J.M., 1997. Seismic attenuation tomography using the frequency shift method, *Geophysics,* **62**(3), 895–905.

Rautian, T. & Khalturin, V., 1978. The use of the coda for determination of the earthquake source spectrum, *Bull. seism. Soc. Am.,* **68**(4), 923–948.

Romanowicz, B., 1998. Attenuation tomography of the Earth's mantle: a review of current status, *Pure appl. Geophys.,* **153**(2–4), 257–272.

Sato, H., Fehler, M.C. & Maeda, T., 2012. *Seismic Wave Propagation and Scattering in the Heterogeneous Earth,* Vol. 496, Springer.

Schurr, B., Asch, G., Rietbrock, A., Trumbull, R. & Haberland, C., 2003. Complex patterns of fluid and melt transport in the central Andean subduction zone revealed by attenuation tomography, *Earth planet. Sci. Lett.,* **215**(1–2), 105–119.

Sharma, B., Teotia, S. & Kumar, D., 2007. Attenuation of P, S, and coda waves in Koyna region, India, *J. Seismol.,* **11**(3), 327–344.

Sketsiou, P., Napolitano, F., Zenonos, A. & De Siena, L., 2020. New insights into seismic absorption imaging, *Phys. Earth planet. Inter.,* **298,** 106337.

Takemura, S., Furumura, T. & Saito, T., 2009. Distortion of the apparent *S*-wave radiation pattern in the high-frequency wavefield: Tottori-Ken Seibu, Japan, earthquake of 2000, *Geophys. J. Int.,* **178**(2), 950–961.

Tertulliani, A. & Cucci, L., 2014. New insights on the strongest historical earthquake in the Pollino region (southern Italy), *Seismol. Res. Lett.,* **85**(3), 743–751.

Tisato, N. & Madonna, C., 2012. Attenuation at low seismic frequencies in partially saturated rocks: measurements and description of a new apparatus, *J. Appl. Geophys.,* **86,** 44–53.

Totaro, C., Koulakov, I., Orecchio, B. & Presti, D., 2014. Detailed crustal structure in the area of the southern Apennines–Calabrian Arc border from local earthquake tomography, *J. Geodyn.,* **82,** 87–97.

Totaro, C., Seeber, L., Waldhauser, F., Steckler, M., Gervasi, A., Guerra, I., Orecchio, B. & Presti, D., 2015. An intense earthquake swarm in the southernmost Apennines: fault architecture from high-resolution hypocenters and focal mechanisms, *Bull. seism. Soc. Am.,* **105**(6), 3121–3128.

Yoshimoto, K., Sato, H. & Ohtake, M., 1993. Frequency-dependent attenuation of *P* and *S* waves in the Kanto area, Japan, based on the coda-normalization method, *Geophys. J. Int.,* **114**(1), 165–174.

SUPPORTING INFORMATION

Supplementary data are available at *GJI* online.

Figure S1. Cross-sections showing the ΔQ_P^{-1} variations at three frequency bands: 3, 6 and 15 Hz for Data set 1. The top single panel shows a map of the area with the seismic events used in this study (red dots) and the seismic stations (blue triangles). Line AA' represents an NW–SE cross-section (second row panels). Line BB' represents an N–S cross-section (third row panels) and line CC' represents an E–W cross-section (bottom row panels), all of them taken through the main swarm. The black circle markers represent the events of the main seismic swarm, the hourglass markers represent the events of the secondary swarm and the open square markers represent the rest of the seismicity in the area. The grey areas are beyond our resolution power and they have been masked for simplification.

Figure S2. Input (right panels) and results (left panels) of two spike tests performed using Data set 1 at a frequency of 3 Hz at 7.5 km depth. The black lines on the panels represent the main faults in the area, adapted from Brozzetti *et al.* (2017).

Figure S3. Cross-sections showing the ΔV_P (left column) and ΔV_S (right column) velocity structure in our area of interest at 3, 7.5 and 12.5 km. The model has been adapted from Totaro *et al.* (2014). The depth is shown at the bottom left corner of each panel. The black lines represent the main faults in the area, adapted from Brozzetti *et al.* (2017).

Please note: Oxford University Press is not responsible for the content or functionality of any supporting materials supplied by the authors. Any queries (other than missing material) should be directed to the corresponding author for the paper.